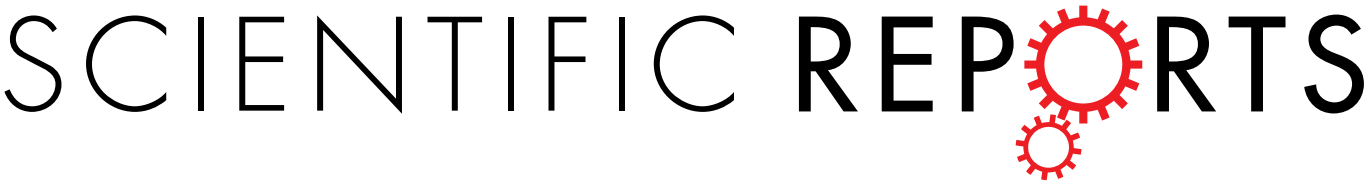

OPEN

Superconducting and normal-state anisotropy of the doped topological insulator $Sr_{0.1}Bi_2Se_3$

Received: 11 December 2017
Accepted: 2 May 2018
Published online: 16 May 2018

M. P. Smylie[1,2], K. Willa[1], H. Claus[1], A. E. Koshelev[1], K. W. Song[1], W.-K. Kwok[1], Z. Islam[3], G. D. Gu[4], J. A. Schneeloch[4,5], R. D. Zhong[4,6] & U. Welp[1]

$Sr_xBi_2Se_3$ and the related compounds $Cu_xBi_2Se_3$ and $Nb_xBi_2Se_3$ have attracted considerable interest, as these materials may be realizations of unconventional topological superconductors. Superconductivity with T_c ~3 K in $Sr_xBi_2Se_3$ arises upon intercalation of Sr into the layered topological insulator Bi_2Se_3. Here we elucidate the anisotropy of the normal and superconducting state of $Sr_{0.1}Bi_2Se_3$ with angular dependent magnetotransport and thermodynamic measurements. High resolution x-ray diffraction studies underline the high crystalline quality of the samples. We demonstrate that the normal state electronic and magnetic properties of $Sr_{0.1}Bi_2Se_3$ are isotropic in the basal plane while we observe a large two-fold in-plane anisotropy of the upper critical field in the superconducting state. Our results support the recently proposed odd-parity nematic state characterized by a nodal gap of Eu symmetry in $Sr_xBi_2Se_3$.

Following the discovery of topological insulators[1,2], the search for a superconducting analogue of a topological insulator has gained considerable interest in the condensed matter physics community. A topological superconductor (TSC)[3–5] has a bulk superconducting energy gap (nodal or nodeless)[6] but has gapless surface states which are of great interest both for fundamental physics, as they can host Majorana quasiparticles[7], and also for applied physics, as the non-Abelian statistics of surface-state excitations have important implications for robust quantum computing[8–10].

The topological nature of the superconducting state is determined by the symmetry of the superconducting order parameter and the shape of the Fermi surface. In a time-reversal and inversion symmetric system, odd-parity pairing, where $\Delta(-\mathbf{k}) = -\Delta(\mathbf{k})$, and a Fermi surface that contains an odd number of time-reversal invariant momenta are necessary requirements[5]. In materials with weak spin-orbit coupling, odd-parity pairing corresponds to spin-triplet pairing; for certain strong spin-orbit coupling systems, unique unconventional superconducting states are possible[11] that may qualify as topological superconductivity. Currently, two paths towards topological superconductivity are being investigated: proximity-induced TSC[7,12,13] at the interface between a conventional superconductor and a topological insulator or a strong spin-orbit coupled semiconductor, respectively, and via chemical doping of bulk topological insulators. Of the superconducting doped topological insulators, the $M_xBi_2Se_3$ family of materials (M = Cu, Nb, Sr)[14–16] has generated the most interest as high quality, mm-scale single crystals are available. Topological order observed via ARPES measurements[17] and magnetization measurements[18,19] is consistent with a spin-triplet pairing state. Calorimetry measurements[20] are not in full agreement with conventional BCS theory, and low-temperature penetration depth measurements[21] indicate nodes in the superconducting energy gap. The observation of zero-bias conductivity peaks in point-contact spectroscopy measurements[22–24] has been interpreted as evidence for Majorana surface states.

The $M_xBi_2Se_3$ family maintains the trigonal $R\bar{3}m$ structure of the parent compound. Following the surprising observation[25] of an anomalous Knight shift in $Cu_xBi_2Se_3$ demonstrating spin-triplet pairing and twofold anisotropy in the threefold symmetric basal plane, a nematic superconducting state with a two-component order

[1]Materials Science Division, Argonne National Laboratory, 9700 S. Cass Ave, Lemont, Illinois, 60439, USA. [2]Department of Physics, University of Notre Dame, Notre Dame, Indiana, 46556, USA. [3]Advanced Photon Source, Argonne National Laboratory, 9700 S. Cass Ave, Lemont, Illinois, 60439, USA. [4]Condensed Matter Physics and Materials Science Department, Brookhaven National Laboratory, Upton, New York, 11793, USA. [5]Department of Physics and Astronomy, Stony Brook University, Stony Brook, New York, 11794, USA. [6]Department of Materials Science and Engineering, Stony Brook University, Stony Brook, New York, 11794, USA. Correspondence and requests for materials should be addressed to M.P.S. (email: msmylie@anl.gov)

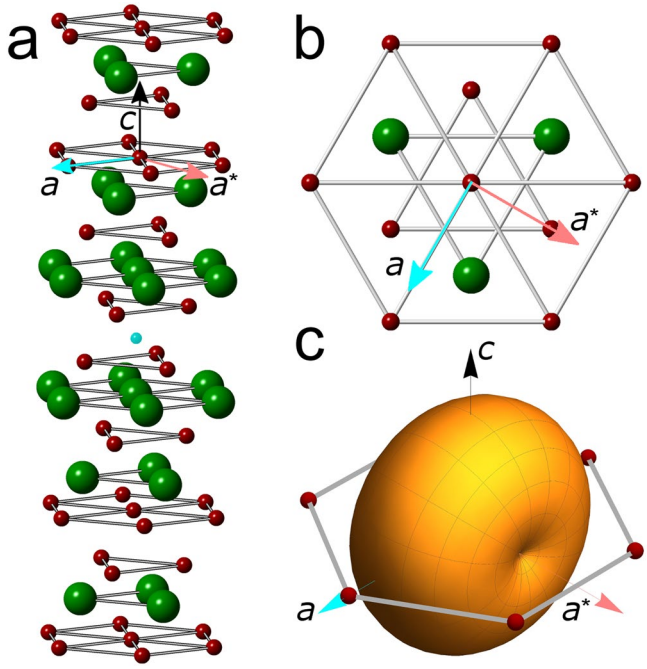

Figure 1. (**a**) Crystal structure of $Sr_xBi_2Se_3$, with directions a (blue), a^* (pink) and c (black) marked. The dopant Sr ion (blue) sits in the van der Waals gap between quintuple layers of Bi (green) and Se (red) ions. (**b**) The threefold symmetric basal plane. (**c**) Schematic presentation of the two-dimensional Δ_4 superconducting gap with respect to a spherical Fermi surface. The Δ_4 gap has basis functions (Δ_{4x}) with nodes on the mirror plane [depicted in (c)] and (Δ_{4y}) with deep minima in the perpendicular direction. This gap breaks the threefold crystal symmetry and gives rise to the nematic state with twofold symmetry.

parameter was proposed[26]. This model[26–28] accounted for subsequent observations of a spontaneous twofold symmetry below T_c in several quantities[29–31] including the upper critical field of $Cu_xBi_2Se_3$ as determined by calorimetry[32] and of $Nb_xBi_2Se_3$ as determined by magnetization[33]. This state has E_u symmetry and odd-parity pairing, and allows for states with complete, albeit anisotropic, superconducting gap as well as for a gap with point nodes. Despite the unconventional nature, the superconducting state has been shown to be robust against disorder scattering[34–36]. Figure 1(a) shows the $R\bar{3}m$ crystal structure of $Sr_{0.1}Bi_2Se_3$, the same as that of the parent compound Bi_2Se_3 with a slightly extended c axis due to intercalation of the Sr atom in the gap between adjacent quintuple layers of Bi_2Se_3[37] while Fig. 1(b) shows the threefold symmetric basal plane, with the a (blue) and a^* (pink) directions marked by arrows. Figure 1(c) shows the proposed twofold symmetric Δ_4 superconducting gap structure, which breaks crystallographic rotational symmetry in the basal plane[26].

Here, we present the first thermodynamic determination of the anisotropy of the upper critical field of $Sr_{0.1}Bi_2Se_3$ single crystals through measurements of the temperature dependence of the reversible magnetization, in addition to angular-dependent magnetotransport measurements. Both quantities yield a large twofold in-plane anisotropy of H_{c2} in which the high-H_{c2} direction is aligned with the a axis of the crystal structure. We find that the normal state resistivity of $Sr_{0.1}Bi_2Se_3$ is isotropic in pairs of samples cut at 90° from the same starting crystal, which excludes conventional mass anisotropy from being the cause of the anisotropy in H_{c2}. Furthermore, temperature dependent measurements of the normal-state magnetization show that $Sr_{0.1}Bi_2Se_3$ is diamagnetic with an isotropic susceptibility of $\sim -2 \cdot 10^{-6}$ (CGS) which largely originates from the core diamagnetism. X-ray diffraction studies indicate that the extinction rule for the $R\bar{3}m$ crystal structure is fulfilled to a level of 10^{-6} implying that deviations from the ideal $R\bar{3}m$ structure are exceedingly small. We thus conclude that the origin of the twofold anisotropy of the superconducting properties is likely caused by an anisotropic gap structure consistent with the nematic E_u state.

Results

We present results on a series of $Sr_xBi_2Se_3$ crystals. Bar-shaped crystals #1a and #1b were cut from the same starting piece oriented at 90° with respect to each other. Field-angle dependent resistivity measurements (Fig. 2) reveal that the nematic state is not tied to the current flow direction. Detailed resistivity measurements as function of applied magnetic field, field orientation and temperature (Figs 3 and 4) on crystal #2 yield the anisotropic phase diagram. On crystal #3 we performed magnetic measurements of the nematic state (Fig. 5) and of the normal state susceptibility (Fig. 6). Bar-shaped crystals #4a and #4b, used for resistivity measurements (Fig. 6), were cut from the same starting piece such that they are oriented parallel and perpendicular to the nematic axis, respectively. High-resolution x-ray diffraction on crystal #2 (Fig. 7) reveals high crystalline quality. Finally, we determined the in-plane superconducting anisotropy using magnetization and resistivity measurements on crystal #5, shown in Supplemental Information.

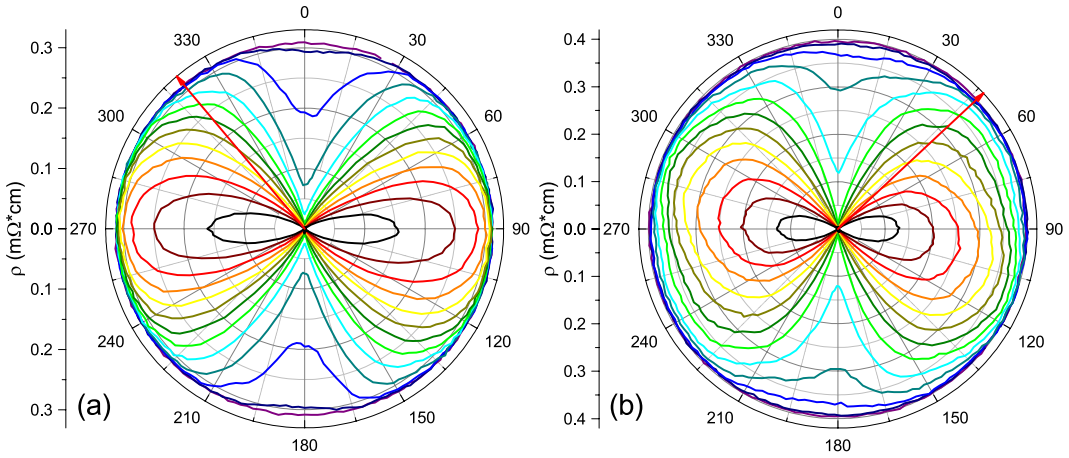

Figure 2. R(θ) in an applied magnetic field of $|H_{ab}| = 10$ kG in two crystals of $Sr_{0.1}Bi_2Se_3$ cut at 90° relative to each other from a single larger crystal in the temperature range 1.7 K (black) to 2.9 K (purple) in 0.1 K steps; $I = 0.1$ mA. 0° marks the crystallographic *a*-axis; the red arrow indicates the direction of current. As temperature increases, the twofold nematic symmetry becomes rotationally isotropic. Rotating the direction of current 90° relative to the crystalline axes results in no change of the nematic axis, demonstrating that vortex motion is not the cause of the observed twofold asymmetry.

The resistivity as a function of in-plane angle in an applied magnetic field of magnitude 10 kG is shown in Fig. 2 for $Sr_{0.1}Bi_2Se_3$ crystals #1a and #1b at temperatures ranging from 1.7 K (black) to 2.9 K (purple) in increments of 0.1 K. The two crystals were cut from the same starting material at 90° with respect to each other (see inset of Fig. 6). Here, the crystals were intentionally cut such that the long axes did not lie along or perpendicular to the nematic axis. 0° in Fig. 2 marks the crystallographic *a* axis. The red arrow indicates the direction of current with respect to the crystal axes. The angular dependence of the resistivity thus reflects the angular dependence of the upper critical field H_{c2}, as directions with higher H_{c2} will remain superconducting whereas directions with lower H_{c2} will be resistive at a fixed temperature. Twofold anisotropy is evident in both Fig. 2(a,b). As temperature is increased from base temperature through the superconducting transition, the twofold anisotropy is eventually lifted, reaching an angle independent normal state. Our observation that the nematic axis does not depend on the direction of the applied current demonstrates that the observed twofold anisotropy is tied to the crystal structure, and is not an effect due to current flow, such as Lorentz force driven vortex motion.

To further investigate the angular anisotropy of H_{c2}, a series of $\rho(T)$ curves were measured on crystal #2 with $T_c \approx 2.9$ K in different applied magnetic fields with the field vector along the directions of maximum and minimum in-plane H_{c2} as well as along the *c* axis of the crystal [Fig. 3(a,b,c)]. X-ray diffraction on this sample (see Fig. 7) reveals that the directions of high (low) in-plane H_{c2} correspond to the crystallographic *a* and a^* directions, respectively (see Fig. 1), consistent with previous reports[29,38]. Figure 3(a,b,c) show that on increasing field the transitions stay sharp and shift uniformly to lower temperatures. A weak normal-state magnetoresistance is observed only for $H//c$. Figure 3(d) shows the magnetic phase diagram along the principal axes with T_c taken as the midpoint of the resistive transitions. The in-plane anisotropy Γ is ~4.5. Reported values for the anisotropy (also determined from the resistive midpoints) range from 6.8 for nominal 10% doping to 2.7 for nominal 15% doping, both at 1.9 K[29], whereas on samples with unspecified doping levels an in-plane anisotropy value of ~2.8 was obtained[38]. In the temperature range covered here, Γ is approximately temperature-independent.

The nematic E_u state that has been proposed as a possible explanation of the twofold anisotropy of superconducting properties is characterized by a two-component order parameter[11,26], which can be expressed as a linear superposition of the two basis gap functions Δ_{4x} and Δ_{4y} (see Fig. 1). An in-depth analysis of the upper critical field of a superconductor with trigonal symmetry and two-component order parameter has been presented in Ref.[39]. Three nematic domains related by rotations of 120° should arise in the sample, giving rise to overall threefold symmetry. Instead, the vast majority of reported data including those presented here reveal a simple twofold anisotropy indicative of a single nematic domain. The theoretical analysis[39] reveals that, in contrast to a single component order parameter, a two component order parameter couples linearly to strain fields as parameterized by a coefficient δ, and that such strain fields may serve to pin the nematic vector into a single domain. In particular, for sufficiently strong pinning δ and near T_{c0}, the two component order parameter is effectively reduced to a single component[33] which for $\delta > 0$ is approximately Δ_{4x} and for $\delta < 0$ it is approximately Δ_{4y}.

In standard single-band Ginzburg-Landau (GL) theory the anisotropy of H_{c2} is given by the anisotropy of the effective masses[40]

$$\frac{H_{c2}^{(i)}}{H_{c2}^{(j)}} = \sqrt{\frac{m_j}{m_i}} = \Gamma > 1 \tag{1}$$

where m_i and m_j are the effective masses along the principal crystal directions *i* and *j*. The unit vectors *i*, *j*, *k* define a Cartesian coordinate system; here, $i = a$, $j = a^*$, $k = c$. The angular variation of H_{c2} in the *ij*-plane is then given by[40]

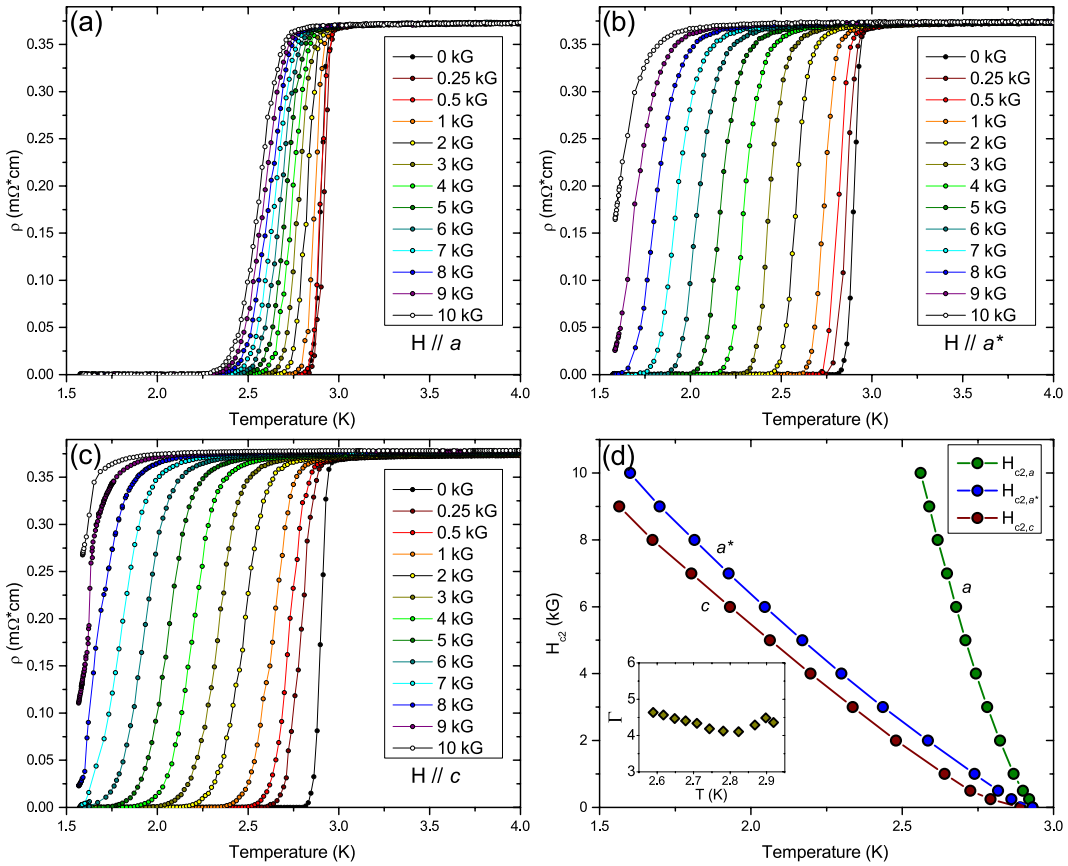

Figure 3. ρ(T) of $Sr_{0.1}Bi_2Se_3$ crystal #2 in increasing magnetic field with the field vector in different orientations. (**a**) Field vector $H//a$. (**b**) Field vector $H//a^*$. (**c**) Field vector $H//c$. (**d**) Magnetic phase diagram. There is a large anisotropy of ~4 between the two in-plane orientations which are 90° apart. The inset shows the in-plane $\Gamma = H_{c2}^{a}/H_{c2}^{a^*}$.

$$H_{c2}(T,\theta) = \frac{H_{c2}^{(j)}}{\sqrt{cos^2(\theta) + \Gamma^{-2}sin^2(\theta)}} \tag{2}$$

where θ is measured from the j-direction (low H_{c2}). Approximating the H_{c2}-line as linear, the angular dependence of $T_c(H,\theta)$ in a given field H can be obtained from Eq. 2 as

$$T_c(H,\theta) = T_{c0} + \frac{H}{\partial H_{c2}^{(j)}(T)/\partial T}\sqrt{cos^2(\theta) + \Gamma^{-2}sin^2(\theta)}\,. \tag{3}$$

Data in a field of $H = 10$ kG are obtained from the polar diagram of $\rho(T,\theta)$ [(Fig. 4(a)] by tracing for which values of T and θ the resistivity crosses the 50% value. The results for $T_c(\theta)$ are shown in Fig. 4(b) together with a fit to Eq. 3. The fit yields an in-plane anisotropy of Γ~3.8, in reasonable agreement with the data in Fig. 3(d). The small difference in anisotropy may arise from deviations from linearity of the phase boundaries.

We obtain the first thermodynamic measurement of the in-plane anisotropy of the upper critical field of $Sr_{0.1}Bi_2Se_3$ from the temperature dependence of the magnetization of crystal #3 with $T_c \sim 3$ K. Figure 5 shows data taken in a field of 4 kG applied along the high- and low-H_{c2} directions, respectively. A shift in T_c, defined as the intersection of a linear fit to the $M(T)$-data with the $M = 0$ line, and a change in the slope dM/dT with field angle are clearly seen. The inset of Fig. 5 displays the twofold symmetric angular variation of the slope dM/dT in which a low value of the slope corresponds to a high value of T_c. Such behavior is expected in conventional single-band GL theory of anisotropic superconductors, for which the slope in field direction i is given as

$$\frac{\partial M^{(i)}}{\partial T} = -\frac{1}{8\pi\beta_A(\kappa^{(i)})^2}\frac{\partial H_{c2}^{(i)}}{\partial T} \tag{4}$$

where $H_{c2}^{(i)} = \phi_0/(2\pi\xi_j\xi_k)$ and $\kappa^{(i)} = \sqrt{(\lambda_j\lambda_k)/(\xi_j\xi_k)} \gg 1$ are the upper critical field and Ginzburg-Landau parameter in direction i, respectively, and $\beta_A = 1.16$ is the Abrikosov number. With the T-linear variation of H_{c2} near T_c one finds that the ratio of the slopes for the high-H_{c2} and low-H_{c2} directions is given by the inverse anisotropy

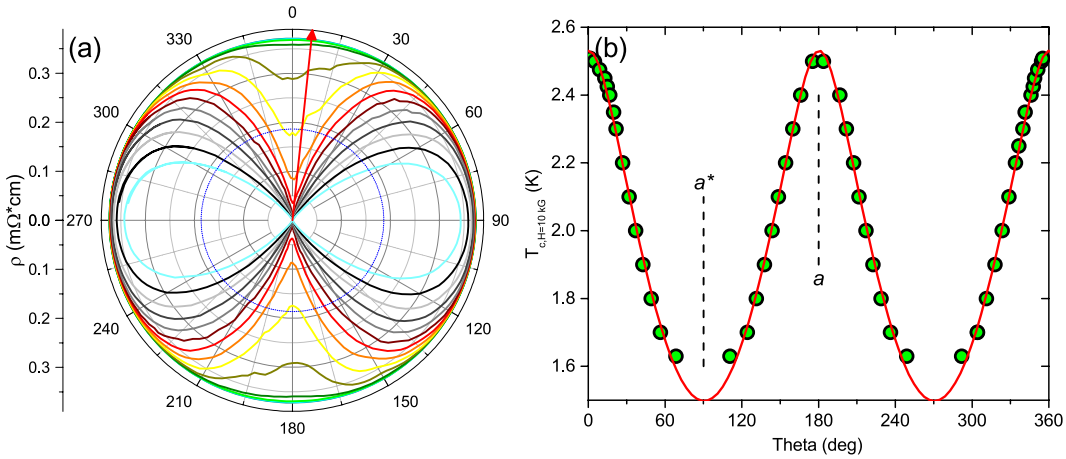

Figure 4. (**a**) $R(\theta)$ for $Sr_{0.1}Bi_2Se_3$ crystal #2 in an applied magnetic field of $|H_{ab}| = 10$ kG in 0.1 K increments, from 1.7 K (cyan) to 3 K (green). 0° marks the *a*-axis; the red arrow, the direction of current. (**b**) $T_c(\theta)$ extrapolated from $R(\theta)$ data for the same crystal, taken as where $R(\theta)$ is half the normal-state value, represented by the blue circle in (**a**). Several additional small θ windows were measured at multiple temperatures to increase data density. The red line is a fit to the data following the Ginzburg-Landau effective mass formula (see text) yielding $\Gamma \approx 3.8$.

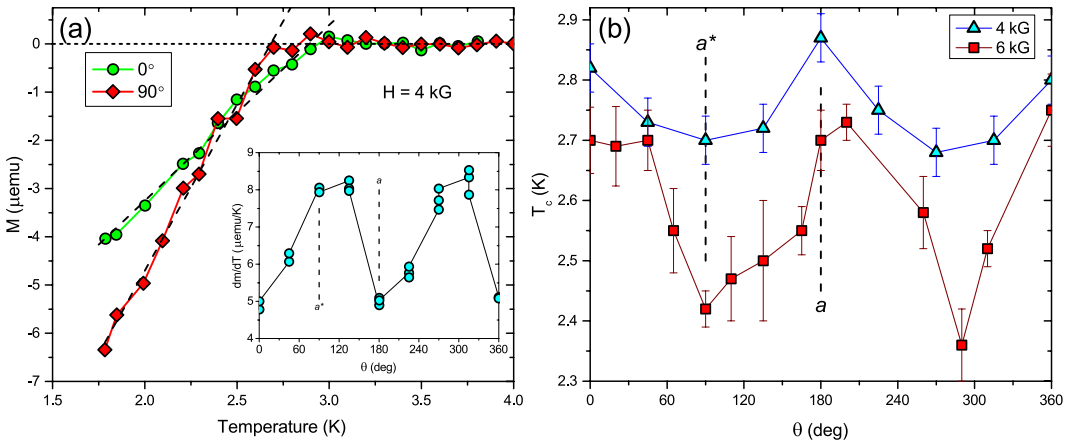

Figure 5. (**a**) $M(T)$ curves as measured by dc SQUID magnetometry on $Sr_{0.1}Bi_2Se_3$ crystal #3 in 4 kG for two different orientations of field 90° apart in the basal plane, with linear fits (dashed lines) below T_c. There is a clear difference in T_c taken as where a linear fit of the response (dashed lines) crosses zero. The inset shows the slope of the linear fit vs angle for multiple measurements. A twofold symmetry in T_c is evident. (**b**) $T_c(\theta)$ with θ the orientation of magnetic field in the basal plane as measured by dc SQUID magnetometry on a single crystal of $Sr_{0.1}Bi_2Se_3$ in fields of 4 kG (blue) and 6 kG (red). In both fields, T_c is again twofold symmetric.

$$\frac{\partial M^{(i)}}{\partial T} / \frac{\partial M^{(j)}}{\partial T} = \frac{\lambda_i}{\lambda_j} = \frac{\xi_j}{\xi_i} = \frac{1}{\Gamma} < 1. \tag{5}$$

Thus, the data shown in the inset of Fig. 5 indicate an anisotropy of $\Gamma \sim 2$ which is smaller than the value deduced from the resistivity measurements (Fig. 3). Data such as shown in Fig. 5(a) taken over the entire angular range in fields of 4 kG and 6 kG yield the angular dependence of T_c as shown in Fig. 5(b) for 4 kG (blue) and 6 kG (red). Although there is sizable scatter in the data [the error bars in Fig. 5(b) reflect the scatter in T_c obtained on repeated runs], a twofold angular symmetry in this thermodynamic determination of T_c is clearly seen consistent with the twofold symmetry observed in magnetotransport measurements. The data shown in Fig. 5(a) also demonstrate that the superconductivity observed in our $Sr_{0.1}Bi_2Se_3$ crystals is a bulk phenomenon and not filamentary.

Although transport and magnetization measurements yield similar qualitative features of the superconducting phase diagram of $Sr_xBi_2Se_3$, i.e. a sizable in-plane anisotropy, there are clear quantitative differences in the value of the anisotropy deduced from both techniques. Generally, such differences may arise since magnetization

and resistivity represent different quantities, the expectation value of the magnitude-squared of the superconducting order parameter and the onset of phase coherence across the sample, respectively. Furthermore, the resistively determined phase boundaries depend on the resistivity criterion used; here we use the 50% criterion. Nevertheless, considering that the resistive transitions shown in Fig. 3 appear 'well-behaved', a difference in anisotropy by a factor of ~2 is surprising. In order to rule out the doping-dependence as a cause of the difference in anisotropy seen in magnetization and magnetoresistance measurements, we performed detailed magnetization and resistivity measurements on a large single crystal, sample #5, shown in Supplemental Information, and reproduce the result that the magnetically determined in-plane superconducting anisotropy is smaller than the resistive result: $\Gamma \sim 2.6$ versus 5. The reasons for this unexpected behavior are not understood at present, and may be related to the unusual positive curvature observed in H_{c2} in all samples as determined by magnetotransport, or to the existence of surface states which may have different superconducting properties[30] than the bulk.

Figure 6(a) shows the temperature dependence of the resistivity of cross-cut crystals with very sharp superconducting transitions at an onset temperature of ~3.0 K oriented such that the current in crystal #4a flows along the a direction and in crystal #4b along a^*, respectively. The anisotropy in the normal-state resistivity is small, <10%. We note that absolute values of the resistivity have an uncertainty of $\sim \pm 15\%$ due to uncertainties in the dimensions of the samples and contact geometry. At the same time, the upper critical field displays a sizable in-plane anisotropy as expressed by the ratio of the effective masses (Eq. 1). For superconductors with essentially isotropic gaps, these effective masses are the same as those entering the normal state conductivity. Our observed sizable in-plane H_{c2}-anisotropy would imply an in-plane resistivity anisotropy of more than 4, which is clearly not consistent with the data shown in Fig. 6. Furthermore, quantum oscillation measurements[41–43] on the Nb and Cu homologues suggest that the planar cross-section of the Fermi surface shows little warping, indicating that effective mass anisotropy cannot be the sole cause of the anisotropy in H_{c2}.

However, for the more general case of anisotropic gaps the GL effective masses are given as[44]

$$\frac{1}{m_i} = \frac{1}{4\pi^3 \hbar N} \oint dS \phi^2(\mathbf{k}) \frac{v_i^2}{v_F} \tag{6}$$

Here, dS denotes an integral over the Fermi surface, N is the electron density, v_i is the i-component of the Fermi velocity, and v_F is the magnitude of the Fermi velocity, both in general $\mathbf{k}$-dependent. $\phi(\mathbf{k})$ describes the anisotropy of the gap over the Fermi surface, normalized such that its Fermi surface average is unity. For instance, for a spherical Fermi surface (isotropic normal state electronic structure) and a model gap anisotropy of $\phi(\mathbf{k}) = \sin(\theta)$ (corresponding to two point nodes on the c-axis) the H_{c2}-anisotropy for fields applied along the c-axis and for fields applied transverse is $1/\sqrt{2}$. We expect that nodal gap structures with different forms of $\phi(\mathbf{k})$ and gaps with deep minima will show similar qualitative behavior, namely, that H_{c2} measured along the line connecting the nodes (minima) is lower than in a transverse direction. This anisotropy can be expressed in terms of the original two-component model[39] as $H_{c2}^{(a)}/H_{c2}^{(a^*)} = \sqrt{(J_1 + J_4)/(J_1 - J_4)}$ for $\delta > 0$ and $H_{c2}^{(a)}/H_{c2}^{(a^*)} = \sqrt{(J_1 - J_4)/(J_1 + J_4)}$ for $\delta < 0$ with an angular dependence that is given by the conventional form (Eq. 2). Here, J_1 and J_4 are coefficients of the gradient terms in the two-component GL free energy in the notation of Ref.[39]. Thus, depending on the values of these coefficients, a sizable temperature independent in-plane anisotropy of H_{c2} can arise even when the electronic structure is essentially isotropic. In particular, our observation that $H_{c2}^{(a)} > H_{c2}^{(a^*)}$ implies that the nodal Δ_{4x} state is realized.

It has been reported that magnetic effects may play an important role in the formation of the superconducting state in Bi_2Se_3-derived superconductors, i.e., $Nb_xBi_2Se_3$[16,45]. We therefore explored the temperature dependence of the normal state magnetization of $Sr_{0.1}Bi_2Se_3$. Figure 6(b) shows data for crystal #3 measured in a field of 10 kG applied along various in-plane directions. Within the experimental uncertainties, the normal state magnetization is isotropic in the basal plane ruling out a magnetic origin of the observed in-plane anisotropy of the superconducting state. Furthermore, in its normal state, $Sr_{0.1}Bi_2Se_3$ is diamagnetic, approaching a volume susceptibility of $-2{\cdot}10^{-6}$ (CGS) at high temperature. The measured magnetic susceptibility, χ, contains several contributions[46], $\chi = \chi_{core} + \chi_P + \chi_L + \chi_{VV} + \chi_{CW}$. Here, χ_{core} represents the core diamagnetism, χ_P and χ_L the Pauli paramagnetism and Landau diamagnetism of the conduction electrons, respectively, χ_{VV} the van Vleck paramagnetism and χ_{CW} a Curie-Weiss contribution, possibly due to magnetic impurities. χ_{core} is temperature independent and isotropic, whereas χ_P, χ_L, and χ_{VV} are temperature independent but in general anisotropic, depending on the band structure and orbital structure. Since the charge count of $Sr_{0.1}Bi_2Se_3$ is much lower than that of typical metals we neglect χ_P and χ_L. With the help of tabulated values[47], χ_{core} of $Sr_{0.1}Bi_2Se_3$ can be estimated as $-2.3{\cdot}10^{-6}$ (CGS). Thus, the observed isotropic diamagnetic response of $Sr_{0.1}Bi_2Se_3$ is in large part caused by its core diamagnetism, which mainly stems from the Se^{2-} ions. The van Vleck contribution may account for the difference between the measured and expected diamagnetic signals, $\chi_{VV} \sim 0.3 \cdot 10^{-6}$ (CGS). In addition, superimposed onto the diamagnetic signal is a paramagnetic contribution, which approximately follows a Curie-Weiss dependence [Fig. 6(b)]. This contribution is also isotropic, and we attribute it to residual magnetic impurities.

Deviations from the ideal $R\bar{3}m$ crystal symmetry have been proposed as possible causes of the twofold anisotropy itself or as mechanism of pinning the nematic vector into one domain. We performed x-ray diffraction studies on the crystals used here in order to search for these effects. These measurements revealed a high-degree of structural coherence and phase purity. The determined room-temperature lattice parameters are $a = 4.146$ Å and $c = 28.664$ Å, consistent with a rhombohedral $R\bar{3}m$ crystal symmetry derived from the Sr-intercalated Bi_2Sr_3 structure[15,37]. Figure 7 shows l scans centered on various (h, 0, l) zones performed on the same crystal whose transport measurements are shown in Figs 3 and 4. Multiple h values are shown; $h = 0$ (green circles), $h = 1$ (blue squares), $h = 2$ (pink triangles). At all (h, 0, l) zones examined, only Bragg peaks for which $2h + k + l = 3n$ is satisfied are observed. This is the extinction rule for the $R\bar{3}m$ structure. The data shown in Fig. 7 reveal that this extinc-

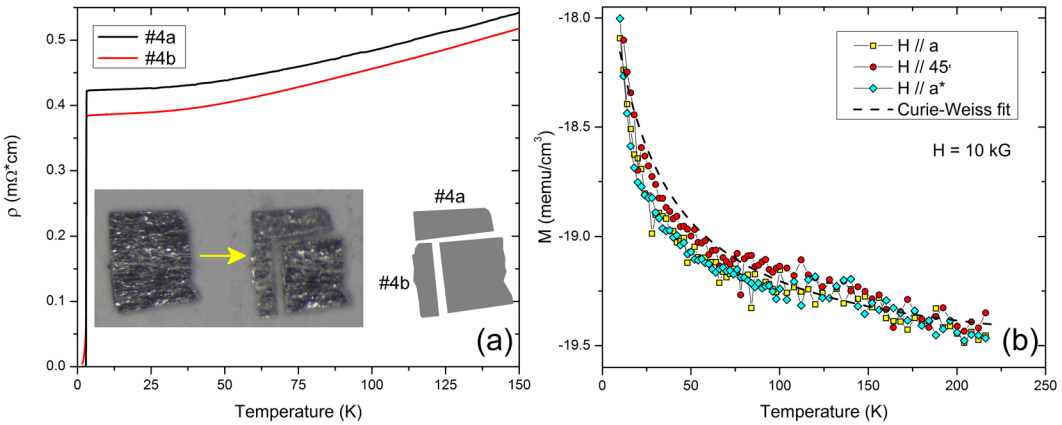

Figure 6. (**a**) Zero-field superconducting resistive transition ($T_c \approx 3.0$ K) of $Sr_{0.1}Bi_2Se_3$ crystals #4a and #4b, cut at right angles to each other out of a single larger crystal. The inset shows a typical ~1 mm^2 crystal before and after cutting two transport samples out of it at right angles to each other. The anisotropy in ρ is within the uncertainty of the dimensions of the electrical contacts. (**b**) Magnetization vs temperature of $Sr_{0.1}Bi_2Se_3$ crystal #3 with the field along the a axis (yellow), the a^* axis (blue), and at 45° to either in the aa^* plane (red). The material is diamagnetic, with a Curie-Weiss component (dashed line) possibly due to impurity contamination. The magnetization is essentially isotropic in-plane.

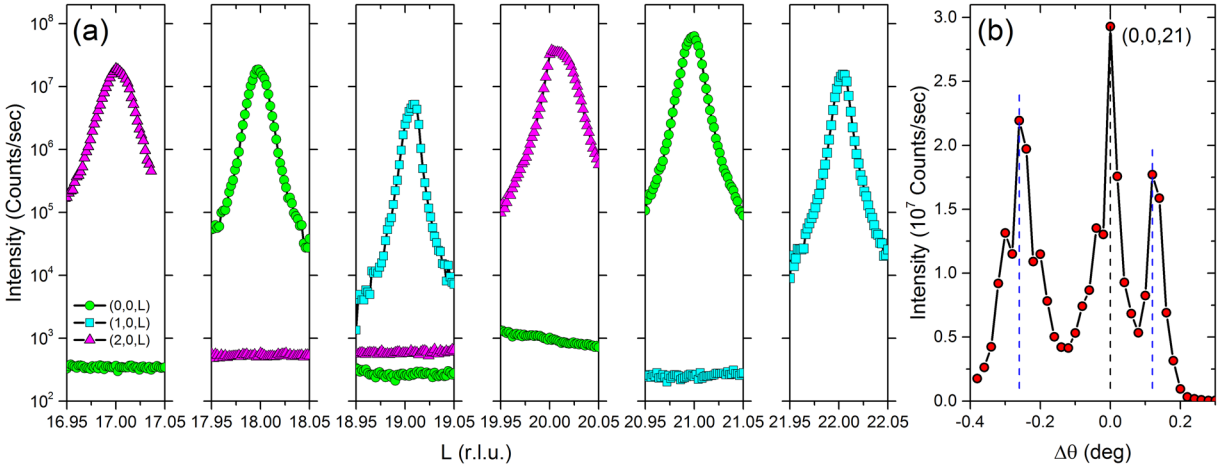

Figure 7. (**a**) Scans centered at (h, 0, l) for multiple values of l on $Sr_{0.1}Bi_2Se_3$ crystal #2 used for transport measurements. Multiple values of h are shown; $h = 0$ (green circles), $h = 1$ (blue squares), $h = 2$ (pink triangles). The trigonal structure enforces an extinction rule unless $2h + k + l = 3n$, where n is an integer. The allowed peaks show approximately 5 orders of magnitude more intensity than at l values that are not allowed, showing the high quality of the crystal. Any distortions away from a perfect crystal structure would appear as violations of the extinction rule; none are seen. An additional crystal examined shows similar results. (**b**) Rocking curve centered at (h, k, l) = (0, 0, 21), showing three closely aligned major grains with a narrow mosaic spread of ~0.04°.

tion rule is satisfied to a level of 10^{-6} implying that deviations from the ideal $R\bar{3}m$ structure are exceedingly small. Over the large illuminated area of the order of 0.4×0.4 mm^2, comparable to the sample size, there are three closely aligned grains with a mosaic of ~0.04° each [see Fig. 7(b)], which is remarkable for a crystal formed from intercalating atoms between stacks of weakly coupled "quintuple layers". These measurements do not reveal, at room temperature, any long-range lattice modulations or compositional variations of Sr that could account for the large twofold anisotropy seen in the superconducting properties. It is unlikely, based on the smooth behavior observed in transport and magnetization data (Fig. 6) and calorimetry data[29], that there is any structural change at low temperature.

Discussion

In addition to angular-dependent magnetotransport measurements we present the first thermodynamic determination of the anisotropy of the upper critical field of $Sr_{0.1}Bi_2Se_3$ crystals through measurements of the temperature dependence of the reversible magnetization. Both quantities yield a large twofold in-plane anisotropy of H_{c2} in which the high-H_{c2} direction is aligned with the a-axis of the crystal structure. Transport measurements on pairs of samples cut at 90° from

the same starting crystal demonstrate that the in-plane anisotropy of H_{c2} is tied to the crystal structure and is not induced by the current flow, consistent with the thermodynamic observations. These measurements also show that the normal state resistivity of $Sr_{0.1}Bi_2Se_3$ is isotropic in the plane, thereby excluding conventional effective mass anisotropy as a cause of the H_{c2}-anisotropy. Furthermore, temperature dependent measurements of the normal-state magnetization reveal that $Sr_{0.1}Bi_2Se_3$ is diamagnetic with an isotropic susceptibility of $\sim -2 \cdot 10^{-6}$ (CGS) which largely originates from the core diamagnetism. These results rule out a possible magnetic origin of the superconducting anisotropy. In addition, x-ray diffraction studies reveal a high degree of structural coherence and phase purity without any detectable deviations from the $R\bar{3}m$ crystal structure that could cause the twofold anisotropy. We thus conclude that the origin of the twofold anisotropy of the superconducting properties is likely caused by an anisotropic gap structure as realized in the nematic E_u state. In fact, by specializing the general form of the GL free energy applicable to the two-component E_u order parameter to the Δ_{4x} and Δ_{4y} basis functions, we retrieve an anisotropic single-component GL expression that can account for the experimental observations, and indicates the Δ_{4x} state is selected.

Methods

Large high quality single crystals of $Sr_{0.1}Bi_2Se_3$ were grown by the melt-growth technique described in Ref.[38]. All crystals regularly showed high volume fraction of superconductivity via magnetic susceptibility measurements with small variation in T_c ranging from 2.9 K to 3.05 K. Thin crystals were cut from as-grown bulk crystals. The material cleaves easily in the basal plane yielding naturally flat surfaces parallel to aa^* in the lattice. Gold contact pads were evaporated, and gold wires were then attached to the crystals using silver epoxy in a conventional 4-point measurement configuration. We typically cut several samples from the same starting piece as shown for example in the inset of Fig. 6(a). After measuring the first sample the overall orientation of the starting piece is known and we can cut all subsequent samples with approximately known orientation such as mutually perpendicular or at arbitrary angles. Some pairs were aligned parallel and perpendicular to the high-H_{c2} direction [such as in Fig. 6(a)] whereas others were intentionally misaligned (such as in Fig. 2). The crystals were mounted with their long axes parallel to each other such that the angle between current and applied in-plane magnetic field were always the same for both. An AMI 10 kG superconducting 3-axis vector magnet was used to apply magnetic field in arbitrary directions without having to physically rotate the sample, and currents smaller than or equal to 1 mA were used for the measurements. Slow rotation of the field direction in 2° increments ensured thermal equilibrium was maintained. The field was swept clockwise from 0° to 400° to eliminate any magnetic hysteresis effects. By recording the magnetoresistance during theta scans (a field with fixed magnitude turning from the z-axis of the magnet into the horizontal plane and beyond) for two azimuthal angles, the orientation of the a-a^* plane of the sample with respect to the magnet can be determined with a precision of less than a degree. Such a small level of planar misalignment cannot account for the large observed in-plane anisotropy of H_{c2}. Magnetization measurements were performed in a 70 kG Quantum Design MPMS with samples mounted on an approximately 25 cm long quartz glass fiber with GE varnish to minimize the background signal. The fiber is suspended from the standard SQUID sample rod which is centered inside the sample chamber with a 7.6 mm diameter spacer ring. The fiber is kept straight with a 7.6 mm diameter plastic weight at the bottom. We estimate that the possible misalignment of this arrangement with respect to the SQUID axis is less than 2°. For angular dependent measurements, the sample is remounted onto the fiber for each angle, which is determined from microscopy photos with a precision of better than 1°. X-ray measurements were performed at the 6-ID-B beamline at the Advanced Photon Source. A vertically focused x-ray beam of 8.979 keV was delivered to the sample. The sample was oriented such that measurements using a reflection geometry from a naturally cleaved surface normal to the *c*-axis can be carried out.

References

1. Hsieh, D. *et al.* A topological Dirac insulator in a quantum spin Hall phase. *Nat.* **452**, 970–974, https://doi.org/10.1038/nature06843 (2008).
2. Hasan, M. Z. & Kane, C. L. Colloquium: Topological Insulators. *Rev. Mod. Phys.* **82**, 3045–3067, https://doi.org/10.1103/RevModPhys.82.3045 (2010).
3. Schnyder, A. P., Ryu, S., Furusaki, A. & Ludwig, A. W. W. Classification of topological insulators and superconductors in three spatial dimensions. *Phys. Rev. B* **78**, 195125, https://doi.org/10.1103/PhysRevB.78.195125 (2008).
4. Qi, X.-L., Hughes, T. L., Raghu, S. & Zhang, S.-C. Time-Reversal-Invariant Topological Superconductors and Superfluids in Two and Three Dimensions. *Phys. Rev. Lett.* **102**, 187001, https://doi.org/10.1103/PhysRevLett.102.187001 (2009).
5. Qi, X.-L. & Zhang, S.-C. Topological insulators and superconductors. *Rev. Mod. Phys.* **83**, 1057–1110, https://doi.org/10.1103/RevModPhys.83.1057 (2011).
6. Schnyder, A. P. & Brydon, P. M. R. Topological surface states in nodal superconductors. *Journal of Physics: Condensed Matter* **27**, 243201, http://stacks.iop.org/0953-8984/27/i=24/a=243201 (2015).
7. Beenakker, C. W. J. Search for Majorana Fermions in Superconductors. *Annu. Rev. Condens. Matter Phys.* **4**, 113–136, https://doi.org/10.1146/annurev-conmatphys-030212-184337 (2013).
8. Wilczek, F. Majorana returns. *Nat. Phys.* **5**, 614–618, https://doi.org/10.1038/nphys1380 (2009).
9. Merali, Z. Quantum Computing: The Power of Discord. *Nature* **474**, 24–26, https://doi.org/10.1038/474024a (2011).
10. Nayak, C., Simon, S. H., Stern, A., Freedman, M. & Das Sarma, S. Non-abelian anyons and topological quantum computation. *Rev. Mod. Phys.* **80**, 1083–1159, https://doi.org/10.1103/RevModPhys.80.1083 (2008).
11. Fu, L. & Berg, E. Odd-Parity Topological Superconductors: Theory and Application to $Cu_xBi_2Se_3$. *Phys. Rev. Lett.* **105**, 097001, https://doi.org/10.1103/PhysRevLett.105.097001 (2010).
12. Albrecht, S. M. *et al.* Exponential protection of zero modes in Majorana islands. *Nature* **531**, 206–209, https://doi.org/10.1038/nature17162 (2016).
13. Mourik, V. *et al.* Signatures of Majorana Fermions in Hybrid Superconductor-Semiconductor Nanowire Devices. *Science* **336**, 1003 http://science.sciencemag.org/content/336/6084/1003.abstract (2012).
14. Hor, Y. S. *et al.* Superconductivity in $Cu_xBi_2Se_3$ and its Implications for Pairing in the Undoped Topological Insulator. *Phys. Rev. Lett.* **104**, 057001, https://doi.org/10.1103/PhysRevLett.104.057001 (2010).
15. Liu, Z. *et al.* Superconductivity with Topological Surface State in $SrxBi_2Se_3$. *J. Am. Chem. Soc.* **137**, 10512–10515, https://doi.org/10.1021/jacs.5b06815 (2015).

16. Qiu, Y. *et al*. Time reversal symmetry breaking superconductivity in topological materials. *ArXiv e-prints* **1512**, 03519 (2015).
17. Wray, L. A. *et al*. Observation of topological order in a superconducting doped topological insulator. *Nat. Phys.* **6**, 855–859, https://doi.org/10.1038/nphys1762 (2010).
18. Das, P., Suzuki, Y., Tachiki, M. & Kadowaki, K. Spin-triplet vortex state in the topological superconductor $Cu_xBi_2Se_3$. *Phys. Rev. B* **83**, 220513, https://doi.org/10.1103/PhysRevB.83.220513 (2011).
19. Nikitin, A. M., Pan, Y., Huang, Y. K., Naka, T. & de Visser, A. High-pressure study of the basal-plane anisotropy of the upper critical field of the topological superconductor $Sr_xBi_2Se_3$. *Phys. Rev. B* **94**, 144516, https://doi.org/10.1103/PhysRevB.94.144516 (2016).
20. Kriener, M., Segawa, K., Ren, Z., Sasaki, S. & Ando, Y. Bulk Superconducting Phase with a Full Energy Gap in the Doped Topological Insulator $Cu_xBi_2Se_3$. *Phys. Rev. Lett.* **106**, 127004, https://doi.org/10.1103/PhysRevLett.106.127004 (2011).
21. Smylie, M. P. *et al*. Evidence of nodes in the order parameter of the superconducting doped topological insulator $NbxBi_2Se_3$ via penetration depth measurements. *Phys. Rev. B* **94**, 180510, https://doi.org/10.1103/PhysRevB.94.180510 (2016).
22. Sasaki, S. *et al*. Topological Superconductivity in $Cu_xBi_2Se_3$. *Phys. Rev. Lett.* **107**, 217001, https://doi.org/10.1103/PhysRevLett.107.217001 (2011).
23. Kirzhner, T., Lahoud, E., Chaska, K. B., Salman, Z. & Kanigel, A. Point-contact spectroscopy of $Cu_{0.2}Bi_2Se_3$ single crystals. *Phys. Rev. B* **86**, 064517, https://doi.org/10.1103/PhysRevB.86.064517 (2012).
24. Kurter, C. *et al*. Andreev Reflection Spectroscopy of Topological Superconductor Candidate $NbxBi_2Se_3$. *ArXiv e-prints* 1707.08516 (2017).
25. Matano, K., Kriener, M., Segawa, K., Ando, Y. & Zheng, G.-q Spin-rotation symmetry breaking in the superconducting state of $Cu_xBi_2Se_3$. *Nat. Phys.* **12**, 852–854, https://doi.org/10.1038/nphys3781 (2016).
26. Fu, L. Odd-parity Topological Superconductor with Nematic Order: Application to $Cu_xBi_2Se_3$. *Phys. Rev. B* **90**, 100509, https://doi.org/10.1103/PhysRevB.90.100509 (2014).
27. Venderbos, J. W. F., Kozii, V. & Fu, L. Odd-parity superconductors with two-component order parameters: Nematic and chiral, full gap, and Majorana node. *Phys. Rev. B* **94**, 180504, https://doi.org/10.1103/PhysRevB.94.180504 (2016).
28. Nagai, Y., Nakamura, H. & Machida, M. Rotational isotropy breaking as proof for spin-polarized Cooper pairs in the topological superconductor $Cu_xBi_2Se_3$. *Phys. Rev. B* **86**, 094507, https://doi.org/10.1103/PhysRevB.86.094507 (2012).
29. Pan, Y. *et al*. Rotational symmetry breaking in the topological superconductor $Sr_xBi_2Se_3$ probed by upper-critical field experiments. *Sci. Rep.* **6**, 28632, https://doi.org/10.1038/srep28632 (2016).
30. Du, G. *et al*. Drive the Dirac electrons into Cooper pairs in $Sr_xBi_2Se_3$. *Nat. Commun.* **8**, 14466, https://doi.org/10.1038/ncomms14466 (2017).
31. Asaba, T. *et al*. Rotational Symmetry Breaking in a Trigonal Superconductor Nb-doped Bi_2Se_3. *Phys. Rev. X* **7**, 011009, https://doi.org/10.1103/PhysRevX.7.011009 (2017).
32. Yonezawa, S. *et al*. Thermodynamic evidence for nematic superconductivity in $Cu_xBi_2Se_3$. *Nat. Phys.* **13**, 123–126, https://doi.org/10.1038/nphys3907 (2017).
33. Shen, J. *et al*. Nematic topological superconducting phase in nb-doped bi2se3. *npj Quantum Materials* **2**, 59, https://doi.org/10.1038/s41535-017-0064-1 (2017).
34. Nagai, Y. Robust superconductivity with nodes in the superconducting topological insulator $Cu_xBi_2Se_3$: Zeeman orbital field and nonmagnetic impurities. *Phys. Rev. B* **91**, 060502, https://doi.org/10.1103/PhysRevB.91.060502 (2015).
35. Michaeli, K. & Fu, L. Spin-Orbit Locking as a Protection Mechanism of the Odd-Parity Superconducting State against Disorder. *Phys. Rev. Lett.* **109**, 187003, https://doi.org/10.1103/PhysRevLett.109.187003 (2012).
36. Smylie, M. P. *et al*. Robust odd-parity superconductivity in the doped topological insulator $Nb_xBi_2Se_3$. *Phys. Rev. B* **96**, 115145, https://doi.org/10.1103/PhysRevB.96.115145 (2017).
37. Shruti, Maurya, V. K., Neha, P., Srivastava, P. & Patnaik, S. Superconductivity by Sr intercalation in the layered topological insulator Bi_2Se_3. *Phys. Rev. B* **92**, 020506, https://doi.org/10.1103/PhysRevB.92.020506 (2015).
38. Du, G. *et al*. Superconductivity with two-fold symmetry in topological superconductor $Sr_xBi_2Se_3$. *Sci. China PMA60* **60**, 037411, https://doi.org/10.1007/s11433-016-0499-x (2017).
39. Venderbos, J. W. F., Kozii, V. & Fu, L. Identification of nematic superconductivity from the upper critical field. *Phys. Rev. B* **94**, 094522, https://doi.org/10.1103/PhysRevB.94.094522 (2016).
40. Lahoud, E. *et al*. Evolution of the Fermi surface of a doped topological insulator with carrier concentration. *Phys. Rev. B* **88**, 195107, https://doi.org/10.1103/PhysRevB.88.195107 (2013).
41. Lawson, B. J. *et al*. Quantum oscillations in $Cu_xBi_2Se_3$ in high magnetic fields. *Phys. Rev. B* **90**, 195141, https://doi.org/10.1103/PhysRevB.90.195141 (2014).
42. Lawson, B. J. *et al*. Multiple Fermi surfaces in superconducting Nb-doped Bi_2Se_3. *Phys. Rev. B* **94**, 041114, https://doi.org/10.1103/PhysRevB.94.041114 (2016).
43. Kogan, V. G. & Prozorov, R. Orbital upper critical field and its anisotropy of clean one- and two-band superconductors. *Reports on Progress in Physics* **75**, 114502, http://stacks.iop.org/0034-4885/75/i=11/a=114502 (2012).
44. Takanaka, K. Upper critical field of anisotropic superconductors. *Solid State Communications* **42**, 123, https://doi.org/10.1016/0038-1098(82)90365-9, http://www.sciencedirect.com/science/article/pii/0038109882903659 (1982).
45. Chirolli, L., de Juan, F. & Guinea, F. Time-reversal and rotation symmetry breaking superconductivity in Dirac materials. *Phys. Rev. B* **95**, 201110, https://doi.org/10.1103/PhysRevB.95.201110 (2017).
46. Johnston, D. C. & Cho, J. H. Magnetic-susceptibility anisotropy of single-crystal $Bi_2Sr_2CaCu_2O_8$. *Phys. Rev. B* **42**, 8710–8713, https://doi.org/10.1103/PhysRevB.42.8710 (1990).
47. Gupta, R. R. Diamagnetic Susceptibility, vol. 16 of Landolt-Börnstein - Group II Molecules and Radicals (Springer, Berlin, 1986).

Acknowledgements

Magnetization and magnetotransport measurements at Argonne were supported by the U.S. Department of Energy, Office of Science, Basic Energy Sciences, Materials Sciences and Engineering Division. M.P.S. thanks ND Energy for supporting his research and professional development through the NDEnergy Postdoctoral Fellowship Program. K.W. acknowledges support through an Early Postdoc Mobility Fellowship of the Swiss National Science Foundation. Work at Brookhaven was supported by the Center for Emergent Superconductivity, an Energy Frontier Research Center funded by the U.S. Department of Energy.

Author Contributions

G.D.G., J.A.S., R.D.Z. sample synthesis. K.W. sample fabrication, magnetotransport measurements, and x-ray diffraction. H.C. magnetization measurements. U.W. magnetization measurements and analysis. A.E.K. and K.W.S., theoretical analysis. Z.I. x-ray diffraction. W.-K.K. experiment design. M.P.S. magnetotransport measurements, analysis, manuscript writing with contributions of U.W. and K.W. All authors reviewed the manuscript.

Additional Information

Supplementary information accompanies this paper at https://doi.org/10.1038/s41598-018-26032-0.

Competing Interests: The authors declare no competing interests.

Publisher's note: Springer Nature remains neutral with regard to jurisdictional claims in published maps and institutional affiliations.